

# Line-imaging velocimeter for shock diagnostics at the OMEGA laser facility

P. M. Celliers,<sup>a)</sup> D. K. Bradley, G. W. Collins, and D. G. Hicks  
Lawrence Livermore National Laboratory, Livermore, California 94550

T. R. Boehly and W. J. Armstrong  
Laboratory for Laser Energetics, University of Rochester, Rochester, New York 14623

(Received 7 April 2004; accepted 26 July 2004; published 2 November 2004)

A line-imaging velocity interferometer has been implemented at the OMEGA laser facility of the Laboratory for Laser Energetics, University of Rochester. This instrument is the primary diagnostic for a variety of experiments involving laser-driven shock-wave propagation, including high-pressure equation of state experiments, materials characterization experiments, shock characterization for Rayleigh–Taylor experiments, and shock timing experiments for inertial confinement fusion research. Using a laser probe beam to illuminate a target, the instrument measures shock breakout times at temporal resolutions as low as 20 ps, and spatial resolution  $\sim 4\ \mu\text{m}$ . For velocity measurements the detection limit is  $<0.1\ \text{km/s}$ , and velocities of interfaces, free surfaces, and shock fronts traveling through transparent media can be measured with accuracies  $\sim 1\%$  over the range from 4 km/s to greater than 50 km/s. Quantitative measurements of the optical reflectance of ionizing shock fronts can also be obtained simultaneously with the velocity measurements. © 2004 American Institute of Physics. [DOI: 10.1063/1.1807008]

## I. INTRODUCTION

Optical diagnostics are the principal means for observing shock-wave experiments generated on large laser facilities. The earliest laser-driven shock-wave experiments studied shock propagation by detecting the thermal luminescence produced when a strong shock breaks through the surface of an opaque stepped target.<sup>1,2</sup> This technique requires the shock to be sufficiently strong that the thermal luminescence is readily detectable after breakout of the shock front; it has been utilized in a number of shock detection studies at high-energy laser facilities.<sup>3–7</sup> Dedicated instruments to perform this kind of measurement have been developed at the NOVA<sup>8</sup> and OMEGA<sup>9</sup> laser facilities.

Active shock detection techniques probe the target with a laser beam and observe, for example, a sharp change in the optical reflectance when a strong shock breaks through the rear surface.<sup>10</sup> Since signal levels are determined by the probe intensity, not by the target luminescence, active probing techniques can be made sensitive to shock strengths that are too weak to produce a strong luminescence signal (usually less than 100 GPa), but also to ultra-high-pressure shocks in the TPa range. Active probing techniques can provide a wealth of information on transport properties, primarily through quantitative measurement of optical reflectance. Measurements of target reflectance with active probes have revealed detailed information on the electrical conductivity of shock-released Al.<sup>11–13</sup>

An obvious development path for active probing methods is to combine them with interferometric detection schemes. Interferometric detection schemes have long been

available for shock-wave studies: displacement and velocity interferometry techniques were first developed on gas gun and explosively driven shock facilities by Barker and others in the 1960s and 1970s,<sup>14–18</sup> leading to the establishment of the velocity interferometer system for any reflector (VISAR)<sup>16</sup> as a standard high-precision velocity diagnostic. The closely related optically recording velocity interferometer system (ORVIS)<sup>19</sup> employed a streak camera to record the data with subnanosecond time resolution. Later, line-imaging variations on these methods<sup>20–24</sup> took advantage of the spatially resolving capabilities of streak camera detectors to encode spatial information. Adapting these techniques to the context of laser-driven targets<sup>22,23,25,26</sup> has enabled precise measurement of the motion of a variety of shock-related phenomena in laser-driven targets, including the motion of free surfaces, of shocked interfaces, and of ionizing shock fronts in a wide variety of transparent media.<sup>27–29</sup>

The active shock breakout (ASBO) system at the OMEGA laser of the Laboratory for Laser Energetics (LLE) in Rochester, NY is a line-imaging velocity interferometer that is used as a general purpose shock diagnostic. In opaque targets it is used to measure shock speeds by detecting breakout times across stepped interfaces at high shock pressures ( $\geq 100\ \text{GPa}$ ), or by detecting the motion of solid and optically reflecting free surfaces at lower shock pressures (few 10s of GPa). In transparent targets it can measure the velocity of reflecting shock fronts directly from the Doppler shift (usually  $>100\ \text{GPa}$ ), or the velocity of an interface behind a transparent window material at lower stresses (e.g., up to 200 GPa behind a LiF window). The instrument can also be used to determine the target reflectance for many experimental situations. The development of this instrument began on the NOVA laser facility at Lawrence Livermore National Laboratory (LLNL).<sup>23</sup> The design was improved and trans-

<sup>a)</sup> Author to whom correspondence should be addressed; electronic mail: celliers1@llnl.gov

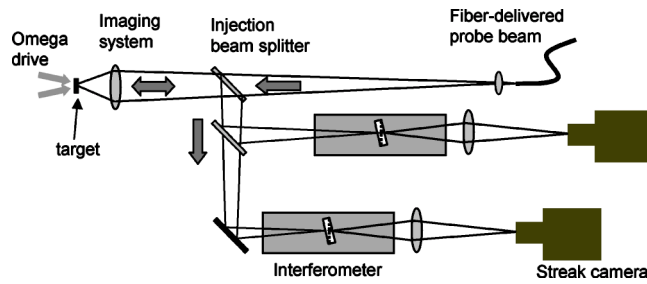


FIG. 1. Conceptual layout of the OMEGA line-imaging shock breakout diagnostic. An image of the target is relayed to the streak cameras through a pair of velocity interferometers.

ferred to the OMEGA laser facility at LLE. Most elements of this design have proven versatile and portable; variations on it have been implemented at the Phebus,<sup>30</sup> Vulcan,<sup>31</sup> and LULI<sup>32</sup> facilities. In this article we describe in detail the design, implementation, and use of this diagnostic at the OMEGA laser facility. We present examples of data collected during recent experiments on the OMEGA laser.

## II. SYSTEM LAYOUT

### A. Overview

At its simplest level the ASBO diagnostic is a high-resolution optical imager that projects a two-dimensional magnified image of the target onto a pair of streak camera detectors (Fig. 1). In somewhat more detail, the system can be divided into a cascade of image relays leading from the

target chamber through a 10 in. diagnostic manipulator and then into the detection paths. The signal passes through a pair of velocity interferometers before being recorded on the streak cameras. The interferometers superimpose a sinusoidal spatial modulation on the image: Doppler shifts in the reflected probe are manifested as shifts of these fringes at the interferometer outputs. The streak cameras record the central chord of the field of view and sweep this signal in time across the output detector.

The probe light is delivered to the diagnostic system through a large-core-diameter multimode fused silica optical fiber, the output of which is collimated and injected into the optical system through a 50% beamsplitter. Light reflected from the target returns to this beamsplitter, from which it is reflected into the detection paths.

### B. Image relays

#### 1. Target to interferometer

The first part of the imaging system, shown in Fig. 2(a), is a pair of telescopes cascaded to produce a magnified real image at the interferometers. The optical elements of this relay comprise a 146 mm objective (L1/L2), a 1675 mm plano-convex singlet (L3, CVI PLCX-1675-50.8), a 1000 mm achromat (L4, CVI AAP-1000-50.8), and a 1675 mm plano-convex (L5, identical to L3). The objective is a compound system with two elements: a 350 mm meniscus (L1, Melles Griot LMP 031) and a 250 mm achromat (L2, CVI AAP-250-50.8). This combination has 146 mm fo-

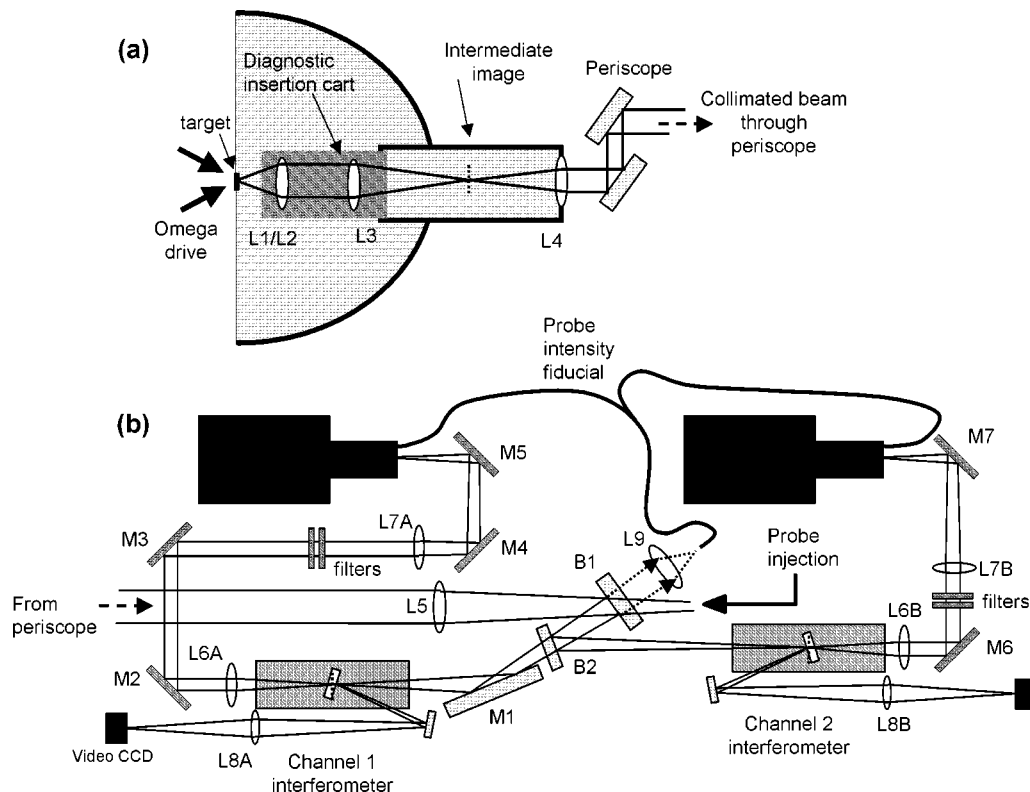


FIG. 2. Details of the image relay system. (a) The front section is a cascade of two image relays with an intermediate image plane localized between L3 and L4. (b) The output image is formed by L5 inside the interferometers, and relayed to the streak cameras through the L6 and L7 pairs of lenses. The probe beam is injected through B1, and the signal path is split into the two channels by B2. (Timing fiducial fibers are not shown.)

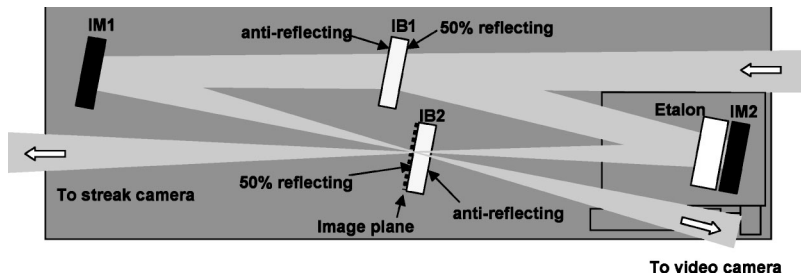


FIG. 3. Detail of the interferometer design. The incoming beam focuses to form an image at the reflecting surface of the output beamsplitter, IB2. Slight tilts of IB2 change the fringe orientation and fringe spacing without affecting contrast. Slight adjustments of the tilt of one of the end mirrors adjust the fringe contrast (image overlap).

cal length and focal ratio  $F/3.3$ . The meniscus also acts as a blast shield to protect the more expensive achromat from target debris, and is replaced every shot. While not achromatic, the  $L1/L2$  combination has close to diffraction-limited performance for the monochromatic probe laser. The point spread resolution at 532 nm is around  $4\text{ }\mu\text{m}$ . The objective collimates the image of the target and transmits it approximately 1 m, where it passes through lens L3. The elements, L1, L2, and L3 are rigidly mounted on the ends of a tube and inserted into the target chamber as a unit. Focusing is achieved by slight axial translations of this tube. An intermediate image plane is situated beyond L3 inside the vacuum housing approximately 1 m from the vacuum window. The next element in the relay is the 1000 mm achromat L4, which also functions as the vacuum window. L4 recollimates the beam for the path segment leading from the vacuum housing and through a periscope system onto the diagnostic table [Fig. 2(b)], where it reaches L5. A set of two beamsplitters and a mirror are placed in the paths beyond lens L5. The elements L1–L5 are each 50 mm in diameter.

The first beamsplitter B1 is required to allow injection of the probe beam into the optical system, and is approximately 50% reflecting system at 532 nm. The output images are formed 1500 mm beyond lens L5 and the interferometers are placed precisely such that these images are simultaneously coincident with the output beamsplitter in each interferometer. Magnification at the intermediate image plane inside the vacuum housing is  $\sim 10\times$  (given by the ratio of focal lengths of L3 and  $L1/L2$ ), while magnification in the second stage of the relay from intermediate image plane to the interferometer plane is  $\sim 1.5\times$ , yielding a total magnification from target to interferometer of  $15.3\times$ .

## 2. Interferometer to streak camera

The interferometers are adjusted to impose a fringe pattern on the beam passing through them, and are aligned such that the fringes are localized at the output beamsplitter plane, coincident with the image formed by L5. The final relay, comprising 300 mm achromats L6A and L6B (CVI AAP-300.0-50.8) and 500 mm achromats L7A and L7B (CVI AAP-500.0-50.8), is laid out in a folded arrangement with the 300 mm achromat placed one focal length from the output beamsplitter to collimate the image, and the 500 mm element placed one focal length from the streak camera slit to reform the image. The fold mirrors (M2–M7) in these final relays are 76 mm diameter.

A pair of narrow-band (3 nm) interference filters are placed in this leg to block thermal emission and any residual 527 nm emission originating from the OMEGA laser. Addi-

tional optional neutral density attenuating filters are also placed here to balance signal levels on the streak cameras.

Total magnification in this stage is  $1.67\times$ , giving a system magnification from the target to the streak camera slit of  $25.5\times$ . The effective field of view at the target plane is approximately  $760\text{ }\mu\text{m}$ . At  $25.5\times$  magnification, the  $4\text{ }\mu\text{m}$  point spread function at the object plane is well matched to the point spread function of the streak tube ( $\sim 100\text{ }\mu\text{m}$ ), and results in  $\sim 200$  spatial resolution elements across the field of view.

## C. Interferometers

The interferometers employ a Mach-Zehnder configuration, shown in Fig. 3, and are constructed on 19-mm-thick aluminum plates placed on three-point kinematic supports. Several interferometer plates are configured at any given time, and the kinematic mounting allows the interferometers to be changed with relative ease between experiments, thus allowing variability in the velocity sensitivities. The distance between the end mirrors is approximately 500 mm, the lateral separation of the beamsplitters is approximately 40 mm, and the angle enclosed between the folded beams is approximately  $9^\circ$ . The optical elements in the interferometers are 25.4 mm diameter: a pair of protected silver mirrors and a pair of 50% beam splitters optimized for 532 nm operation. The interferometer is designed to produce a precise delay in one of its arms. The end mirror and the etalon in the delay arm of the interferometer are both mounted on a motorized translation stage. The encoded motor can move the stage to arbitrary positions with  $\mu\text{m}$  precision. The optical delay is achieved by a combination of the refractive delay in the etalon and an additional translational offset of the etalon-mirror combination along a direction perpendicular to the mirror plane. The translation distance,  $d=h(1-1/n)$ , is calculated to place the image of the mirror plane as viewed through the etalon coincident with its initially determined null position (i.e., zero path delay with the etalon removed, see Sec. II C 1 and the Appendix). The resulting optical time delay is<sup>16,33</sup>

$$\tau = \frac{2h}{c}(n - 1/n), \quad (1)$$

where  $h$  is the etalon thickness,  $n$  is the index of refraction of the etalon, and  $c$  is the speed of light. The etalon elements are made of UV-grade fused silica with antireflection coatings for 532 nm on both surfaces. In some cases a delay of a given thickness is achieved by stacking two or more such pieces into the mounting barrel.<sup>34</sup> Total etalon thickness can vary from 2 up to 60 mm, corresponding to velocity sensi-

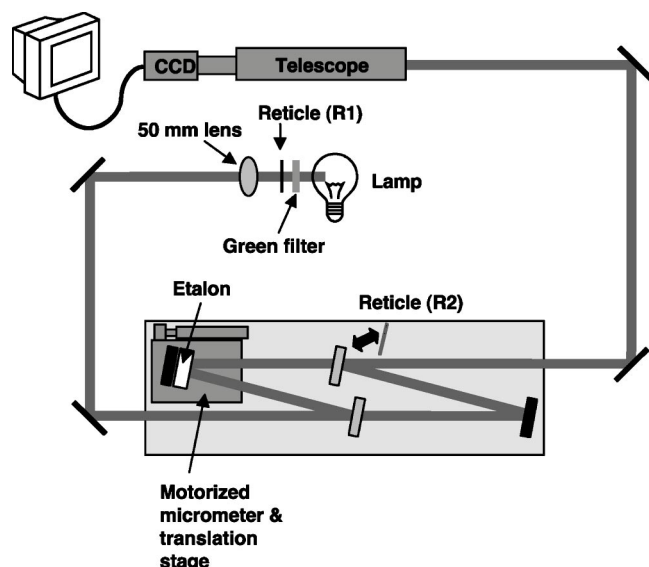


FIG. 4. Arrangement used for interferometer alignment. The telescope is used to view precisely through the centers of all the apertures in the interferometer, and to detect the presence of white light fringes localized at the reflecting surface of the output beamsplitter when the path lengths of the two arms are equalized.

tivities ranging from 25 to 0.86 km/s/fringe, respectively (see Sec. IV).

### 1. Setup and alignment

Alignment and installation of etalons in the interferometers is accomplished at a workstation away from the target area. The alignment procedure is designed to produce a setting for the optical delay that is accurate to a few microns in optical path; this is critical for ensuring the accuracy of the measurements. The alignment procedure also ensures that the optical axis of the interferometer is set reproducibly. The alignment workstation, shown in Fig. 4, comprises a telescope fitted with a video CCD to allow precise viewing of the various optical elements inside the interferometer, a white light source (tungsten lamp), a broadband green filter (centered around 540 nm) illuminating a reticle R1, and a 50 mm single-lens reflex (SLR) camera lens. The SLR lens projects an image of the reticle into the interferometer. In addition two alignment aids are used: a reticle R2 fitted into a custom fixture such that it can be placed precisely in the center of and adjacent to the active surfaces of the beam splitters within the interferometer, and an aluminum disk with center markings that can be substituted into the mounts holding the end mirrors.

The main steps to align the interferometers are: (1) set the angles of all four elements in the interferometer precisely such that the optical axis is centered on the four elements; (2) match the path lengths of the two paths in the interferometer to within  $1.5 \mu\text{m}$ ; and (3) install the delay etalon and translate the adjustable leg precisely to the offset required for the given delay element. Each etalon thickness  $h$  is measured with  $\pm 10 \mu\text{m}$  uncertainty using both a micrometer and a phase-stepping white light interferometer. Using the known index of refraction  $n=1.4607$  for UV-grade fused silica at 532 nm, we can compute the translation offset  $d$  to approxi-

mately  $\pm 3 \mu\text{m}$  uncertainty. In practice, the optical path delay is known to  $\pm 10 \mu\text{m}$  uncertainty ( $\pm 30$  fs), limited primarily by the reproducibility of the translation stage. A more detailed description of steps (1) and (2) is given in the Appendix.

### 2. Fringe adjustments

When perfectly aligned (parallel output beams), the Mach-Zehnder interferometer has a uniform output intensity: a single phase across the output. For the line-imaging application, a fringe comb is imposed on the output by slightly tilting the output beamsplitter, thus imposing a linear ramp in relative optical path difference across the output field. Doppler shifts in the light passing through the interferometer result in changes in the optical phase at the output, and these in turn appear as shifts in fringe position. The spatial frequency of this imposed pattern is arbitrary and is usually set to provide from 12 to 25 fringes across the output image (corresponding to a range of 8 to 16 spatial resolution elements per fringe).

We chose the Mach-Zehnder design with the image plane situated on the output beamsplitter for several reasons. By separating the splitting and recombining of the two paths into two elements, our arrangement employs conveniently small and inexpensive 25.4-mm-diameter optical elements. The arrangement is symmetrical, because the active surfaces of the beamsplitters can be arranged to cancel out the additional delays introduced by the beamsplitter substrates (each path passes through the substrate once, which is not the case with the Michelson geometry), and this symmetry simplifies our path length zeroing procedures. By placing the image plane at the output beamsplitter, we decouple adjustments that optimize fringe contrast from adjustments that change fringe orientation and fringe spacing. All of these adjustments can be made through a wide range of settings not limited by the relatively small 20 mm clear aperture of optical elements in the system. Fringe contrast depends primarily on the degree to which the images projected through the two arms of the interferometer are overlapped. This is easily optimized by slight adjustments of one of the end mirrors in the interferometer. The fringe orientation and spacing are controlled by slight tilt adjustments of the output beamsplitter; since the image is located precisely on the output beamsplitter plane, this adjustment does not affect the image position (i.e., overlap), and therefore does not affect the fringe contrast.

There is one obvious disadvantage of this design: for some alignment tasks we place a reticle fixture (identical to R2 in Fig. 4) on the beamsplitter to provide an object that can be imaged onto the detectors (see Sec. II D). By placing these alignment aids on this surface, the beamsplitter is susceptible to being scratched or contaminated; these defects will appear in the detected images, since they are in focus. However, we believe that this problem is minor, because these defects are much smaller (few  $\mu\text{m}$ ) than the spatial resolution at the streak camera detector plane ( $\sim 100 \mu\text{m}$ ), and are not apparent in the detector images. Since the interferometer elements are small, they are inexpensive and can be replaced easily if necessary.



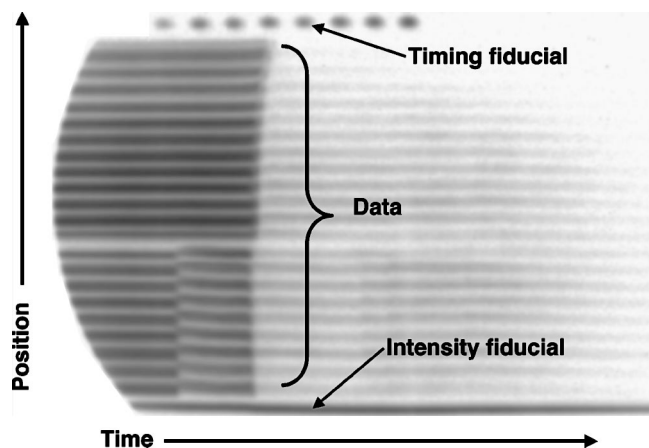


FIG. 5. Arrangement of fiducial traces recorded on the edges of a data record. The fiducial signals are injected at the cathode slit using a pair of 100  $\mu\text{m}$  core diameter optical fibers.

#### D. Alignment monitors

Each interferometer produces two outputs. The main output channel is the beam that passes through the output beamsplitter parallel to and in the same direction as the input beam. The second output is formed from the beams that exit the interferometer at an angle of approximately  $9^\circ$  from the input direction. This output is effectively identical to the signal output and carries the same image (but with inverted fringes). For each interferometer, the second output is re-imaged onto the detector plane of a video CCD camera, using a 300 mm achromat (L8a and L8b).

The video CCD camera is used to view the target during alignment procedures prior to a target shot. The success of this arrangement depends on the accuracy of the registration of the video image relative to the image projected onto the streak slit. We check this registration by placing an alignment reticle at the output beamsplitter plane of each interferometer and illuminating it with a low-power cw alignment beam. By centering the two output images simultaneously on the video monitor and the streak camera slit, we can ensure that the target images viewed in the monitor are accurately registered onto the streak camera. The images viewed in the monitors can be used to perform *in situ* interferometer fringe adjustments (fringe contrast, spacing, and orientation).

#### E. Timing and intensity fiducials

In order to take the most advantage of the data available in the streak record (timing, velocity from fringe shift, and shock reflectance from intensity), two fiducials are imposed onto the edges of each data record, as shown in Fig. 5. The first is the standard OMEGA timing fiducial containing eight timing pulses with  $\sim 0.5$  ns spacing (the pulse pattern and its timing are known very precisely and can be used for sweep rate calibration and time registration). The second is an intensity fiducial which records the intensity of the probe pulse that is delivered to the diagnostic from the probe laser during the shot. The intensity fiducial is extracted by collecting the probe light reflected from the injection beamsplitter B1 using a 50 mm SLR lens (L9). This light is focused into a 100  $\mu\text{m}$  multimode fiber (same fiber type as the timing fiducial fiber)

and delayed through approximately 12 m of optical fiber before it is extracted and injected into the slits of the streak cameras. This delay is designed to match the path delay of the probe to the target chamber and back. By comparing the reflected probe beam intensity to the intensity fiducial, one can extract information about the reflectance of the target during the shot.

### III. TARGET ILLUMINATION

#### A. Probe laser

VISAR experiments require a relatively high-power single-frequency probe beam. The duration of most laser-driven shock experiments is a few nanoseconds to several tens of nanoseconds at most. After accounting for losses the power levels, required to produce good exposure on a streak camera during a time window of a few nanoseconds can exceed 5 kW. We have found a good choice for generating the probe beam to be an injection-seeded frequency-doubled Q-switched Nd:YAG laser source with  $\sim 10$  ns pulse duration. The primary advantage of using a pulsed laser is that high output power is easily available, it is possible to adjust the probe beam intensity to the required levels by attenuating filters, and it is relatively easy to synchronize the Q-switch of the probe laser with OMEGA timing system.

The probe laser power delivered to the diagnostic table is approximately 30 kW, or 200  $\mu\text{J}$  per pulse in the 10 ns full width of half-maximum pulse. This power level is far lower than the peak power available from the laser, so most of the beam is attenuated prior to injection in the fiber. Using the resulting power level still requires attenuation with optical density 1–1.5 to obtain nonsaturating signal levels on most experiments. A filter wheel located at the fiber output (not shown in Fig. 2) is used to control the power injected into the system. Some targets are not highly reflecting, and the extra available power allows one to extract signals from low-reflecting target surfaces.

#### B. Fiber-coupled illumination

The probe laser light is delivered to the diagnostic station through a 1 mm core diameter, 0.16 numerical aperture, multimode fused silica optical fiber. This fiber-coupled arrangement has two advantages. First, it allows us to place the laser head and associated injection optics in a remote location (possibly a different room from the target area). Second, it is a convenient way of producing a spatially smooth source distribution over a well-defined numerical aperture. Spatial mode mixing through the long delivery path ( $\sim 30$  m) of the multimode fiber results in the formation of a random speckle pattern on the output surface of the probe delivery fiber. On average, the probe beam intensity is highly uniform across the output face of the fiber, and its angular distribution is also uniform within the solid angle defined by the numerical aperture of the fiber. On very small spatial scales ( $\sim$  few  $\mu\text{m}$ ), the beam is highly modulated. The spatial scale of the speckles is similar to the resolution limit of the optical system, while feature sizes of interest in our experiments are 10–100 times larger than this. The probe beam is collected and collimated by a 50 mm lens on the diagnos-

tic station, after which it is injected into the optical path through the input beamsplitter. The probe beam illuminates the target over an area  $\sim 1$  mm in diameter, which matches the diameter of the laser drive beams used in shock experiments.

Many of our experiments observe reflecting shock fronts propagating through a transparent medium; these shocks behave as high quality *specular* reflectors with some curvature. The curvature of the shock front is minimized by using a smooth, flat irradiation pattern in the drive beams. In the center of the shock, the curvature ranges typically from  $\sim 1$  cm to a few cm radius. These curvatures are small relative to the relevant scales of the laser driven shock experiments ( $\sim 0.8$  mm spot diameter and  $< 100$   $\mu$ m propagation distance), so from the point of view of the shock physics, one-dimensional motion is well approximated. However, relative to the optical system an optical surface with a  $\sim 1$  cm radius has a large optical power (effective focal length much shorter than the focal length of the imaging optics), and can increase the divergence of the reflected beam significantly. This is the primary reason for combining the relatively fast  $F/3.3$  collection optic with the multimode illumination: The multimode illumination beam fills the numerical aperture of the imaging and collection optic completely and thereby samples the target surface at all possible angles of incidence allowed by the numerical aperture of the optic over the full diameter of the illuminated region. This maximizes the probability of returning the signal through the optical train, even for specular shock fronts with significant curvature.

### C. Depth of field

The relatively fast optic used for our experiments limits the depth of field over which the reflecting surface remains in sharp focus. For experiments during which the reflector travels beyond the range of sharp focus, the observed data will represent a spatially averaged velocity. This situation must be taken into account when interpreting results from a given experiment.

For external surfaces, the depth of field is limited to about 25  $\mu$ m, as defined by the amount of defocus required to make the geometric blur spot comparable to the best focus point spread function. For reflections originating within a refracting sample, the cone angle of collected light internal to the sample is reduced, so that the effective depth of field is larger, by a factor related to the index of refraction of the sample, for example, 40  $\mu$ m in quartz. While this depth of field is still relatively small, many measurements take place on axial scale lengths not much larger than this: usually in the range of 25 to 100  $\mu$ m. For example, shock-wave impedance-matching experiments employ step heights typically ranging from 10 to 40  $\mu$ m, which is comparable to the depth of field.

## IV. VELOCITY SENSITIVITY

The velocity sensitivity of VISAR systems is often quoted as the velocity per fringe, or VPF. For VISARs with glass delay elements, it is given by<sup>16,35</sup>

$$\text{VPF}_0 = \frac{\lambda}{2\tau(1 + \delta)}, \quad (2)$$

where  $\tau$  is given by Eq. (1) and the correction term  $\delta$  accounts for dispersion in the etalon (at 532 nm in fused silica  $\delta=0.0318$ ). This sensitivity formula applies for Doppler shifts observed from free surfaces moving in vacuum. For many experiments this situation is not the case, and additional corrections must be factored in depending on details of the experiment.

### A. Sample-dependent corrections

When the reflection originates at an interface viewed through a transparent shocked window, an additional correction factor must be applied, leading to the modified VPF expression<sup>15</sup>

$$\text{VPF}_w = \text{VPF}_0(1 + \Delta\nu/\nu_0)^{-1}. \quad (3)$$

Here, the term  $\Delta\nu/\nu_0$  depends on the refractive index in the shock-compressed window. Correction terms have been empirically determined for several windows, including fused silica,<sup>15,36</sup> LiF,<sup>37</sup> sapphire,<sup>15,36</sup> alpha-quartz,<sup>38</sup> and poly (methylmethacrylate).<sup>15</sup>

When the reflected beam originates from a shock front in flight inside a transparent dielectric medium, the Doppler shift depends on the refractive index in the sample, and the sensitivity becomes

$$\text{VPF}_s = \text{VPF}_0 n_s^{-1}. \quad (4)$$

where  $n_s$  is the index of refraction of the *unshocked* material, just ahead of the shock front. This sensitivity formula can be derived using optical path difference arguments. We have tested this sensitivity formula directly by tracking the shock front in a transparent medium as it travels across a known thickness. Using the VISAR measurement one can compute the integral

$$X_v = \int_{t_0}^{t_1} \text{VPF}_s f(t) dt, \quad (5)$$

where  $f(t)$  is the fringe count observed between the time  $t_0$ , when the shock enters the medium, and the time  $t_1$ , when it exits. The result  $X_v$  should match an independent measurement of the thickness of the sample. We have tested this equivalence in a variety of materials (liquid deuterium, water, alpha-quartz, and diamond), independent measurements of the sample thickness match  $X_v$  to within measurement uncertainties, thus providing an experimental verification of Eq. (4).<sup>39</sup>

From Eq. (4) it is evident that knowledge of the refractive index of the unshocked sample is important to determine shock velocities. This situation implies that any effects that can modify the optical properties of the sample material in the region ahead of the shock front may introduce additional apparent Doppler shifts that are unrelated to the shock velocity (e.g., x-ray photoionization or preheating). These possibilities have to be scrutinized on a case-by-case basis.

## B. Doppler corrections for a fast lens

The  $F/3.3$  lens used for target illumination and signal collection is a relatively fast optic, and the light interacting with the target is distributed over a range of angles, up to  $\sim 9^\circ$  incidence. It is well known that the Doppler shift imparted to the reflected beam is proportional to  $\cos(\theta_i) + \cos(\theta_r)$ , where  $\theta_i$  ( $\theta_r$ ) is the angle of incidence (angle of reflection); however, the VISAR sensitivity formulas assume that the light interacts with the reflecting surface at normal incidence. In order to achieve high accuracy measurements it is therefore important develop a further correction that takes the angular distribution into account.

Fast optic corrections for VISAR experiments have been worked out previously by Sweatt and Crump,<sup>40</sup> who found a linear correction to the VPF, given by

$$\sigma_{sc} = \frac{\epsilon}{2} + \frac{\epsilon^2}{6(1-\epsilon)}, \quad (6)$$

where  $\epsilon = (1 - \cos \beta)/2$ , and  $NA = \sin \beta$  is the numerical aperture of the collection optic. (There is an additional non-linear term that is  $O(\epsilon^4)$ , small enough to be neglected.) The analysis of Sweatt and Crump assumed that a collimated illumination beam interacted with a diffusely reflecting target surface in vacuum at normal incidence ( $\theta_i = 0$ ) and was scattered according to a Lambertian distribution into the aperture of the collecting lens. The Sweatt and Crump correction to the VPF is  $VPF \rightarrow VPF(1 + \sigma_{sc})$ ; for an  $F/3.3$  ( $NA = 0.149$ ) lens this correction is small:  $\sigma_{sc} = 0.003$ .

Our experimental geometry differs from the assumptions of Sweatt and Crump in three important ways. Firstly, the incident beam fills the collection lens over its full aperture, thus sampling the target with a uniform distribution over all possible angles of incidence allowed by the lens; secondly, the reflecting surface is a specular reflector in most cases; and finally, the reflecting surface is often embedded within a refracting sample medium (a shock front in flight in the sample, or a reflecting interface behind a transparent window). The last difference means that the local angle of incidence at the reflecting surface is smaller than its external value owing to refraction, and the correction therefore depends on the index of refraction in the sample at the point where the reflection takes place. We have applied the method of analysis outlined by Sweatt and Crump to this new context and find that the appropriate formula for the Doppler error is, to a very good approximation, given by

$$\sigma_F = \epsilon_F + \frac{\epsilon_F^2}{3(1 - \epsilon_F)}, \quad (7)$$

where  $\epsilon_F = \{1 - \cos[\arcsin(NA/n_s)]\}/2$ , depends on the index of refraction  $n_s$  at the reflecting surface as well as the numerical aperture (NA) of the collection optic. For  $n_s = 1$  (vacuum free surface),  $\sigma_F = 2\sigma_{sc}$ . It turns out that  $\sigma_F$  is largely independent (to within 1%) of the scattering properties of reflector (specular or diffuse Lambertian). Thus, we find that a general expression that takes into account finite numerical aperture (fast lens) effects for our illumination geometry is

$$VPF_F = VPF_x(1 + \sigma_F), \quad (8)$$

where  $x$  indicates either  $w$  or  $s$ , corresponding to the two cases [Eqs. (3) and (4)]. The fast lens tends to reduce the apparent fringe count from its normal incidence value, and therefore the corrected VPF is slightly larger. The worst case is reflection at a vacuum interface ( $n_s = 1$ ), for which  $\sigma_F = 0.006$ . The magnitude of this correction is somewhat smaller than, but comparable to, our estimated measurement accuracy (about 1% for a measurement at around seven fringes, see Sec. V B). Therefore, this correction is of no consequence for most situations. However, we anticipate improved detection methods in the future (e.g., push-pull quadrature recording), in which case these corrections will become important as measurement accuracy improves.

## V. DATA REDUCTION

### A. Phase extraction

The interferograms recorded in all of our experiments are analyzed to extract fringe phase as a function of space and time. Several methods have been proposed for extracting phase information from interferograms of this type, including fringe tracking and global analysis,<sup>41</sup> an approximate push-pull quadrature reduction method,<sup>24</sup> nonlinear fitting<sup>42</sup> (which we used in early work), and the Fourier transform method (FTM) introduced by Takeda *et al.*,<sup>43</sup> as well as variations on FTM developed by many others.<sup>44-46</sup> We have found that the most effective phase extraction method is a variation of FTM. There is an extensive literature on this technique, so we will only briefly describe the steps we use to extract the phase. The FTM begins by assuming that the recorded fringe intensity can be represented as a real-valued function, given by

$$S(x, t) = B(x, t) + A(x, t) \cos[\phi(x, t) + 2\pi f_0 x + \delta_0]. \quad (9)$$

The term  $2\pi f_0 x + \delta_0$  represents the linear phase ramp of the background fringe pattern: this can be thought of as a carrier wave with spatial frequency  $f_0$  and arbitrary phase offset  $\delta_0$ . (For the purposes of this discussion, the background pattern is assumed to maintain a constant fringe frequency  $f_0$ ; in practice,  $f_0$  varies slightly over  $x$  owing to imperfections in the interferometer optics, and distortions introduced by the streak camera.) The data are encapsulated in  $\phi(x, t)$ , which is a phase modulation superimposed on the carrier wave. The function  $B(x, t)$  represents a slowly varying background intensity, or the average unmodulated signal intensity, while  $A(x, t)$  represents the fringe amplitude, such that  $|A| \leq B$ . An equivalent representation of Eq. (9) is

$$S(x, t) = B(x, t) + C(x, t) \exp(2\pi i f_0 x + i \delta_0) + c.c., \quad (10)$$

where  $C(x, t) = A(x, t) \exp[i\phi(x, t)]/2$ . Taking a one-dimensional spatial Fourier transform at fixed time yields

$$s(f, t) = b(f, t) + c(f - f_0, t) + c^*(f + f_0, t), \quad (11)$$

which separates the background function  $b(f, t)$  from the phase information contained in  $c$ . The FTM proceeds by choosing a filter that selects a broad range of the power spectrum around the  $c$ -lobe at positive frequencies and zeroes out the information at all other frequencies (including the nega-



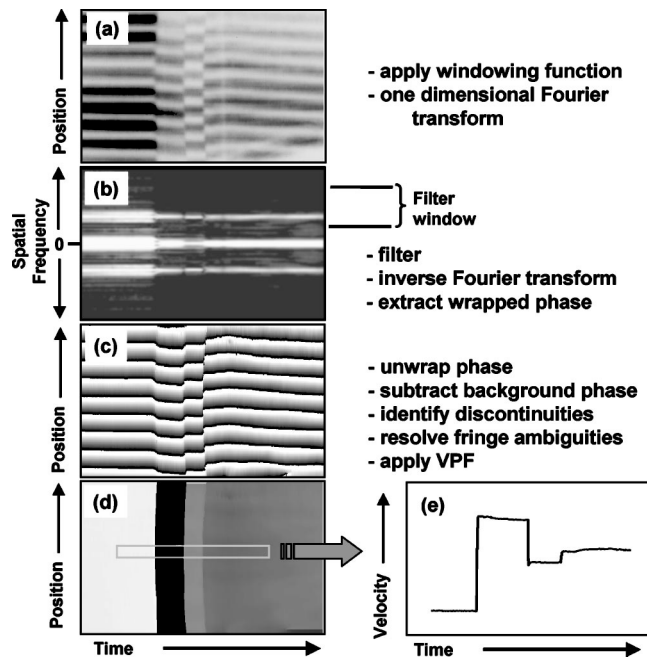


FIG. 6. Main steps if the phase extraction procedure using the Fourier transform method. Shown in the panels are (a) the raw data, (b) the discrete Fourier spectrum, (c) the wrapped phase function  $W$  [Eq. (13)], (d) the final velocity field, and (e) a lineout extracted from the velocity field.

tive  $c^*$ -lobe). Back transforming produces the complex-valued function

$$D(x, t) = C(x, t) \exp[2\pi i f_0 x + \delta_0]. \quad (12)$$

A “wrapped” phase can be extracted from this complex valued function, as

$$W[\phi(x, t) + 2\pi f_0 x + \delta_0] = \arctan[\text{Re}(D), \text{Im}(D)]. \quad (13)$$

The wrapped phase function  $W$  is bounded in the interval  $[-\pi, \pi]$ , resulting in discontinuities when the phase passes through odd multiples of  $\pi$ . The final two steps are to unwrap the phase (remove the  $2\pi$  discontinuities), and to subtract the the background, that is,  $2\pi f_0 x + \delta_0$ , leading to the extracted phase. A graphical illustration of this procedure showing the main steps is shown in Fig. 6.

Although the spatial resolution of the imaging system is  $\sim 4 \mu\text{m}$ , the effective spatial resolution for velocity measurements is lower. This is easily seen within the context of the FTM because of the bandpass spatial filter that is applied to extract the fringe phase. As a consequence, the effective resolution depends on both the interferometer setting (number of fringes) and the filter bandwidth used in the phase extraction process, both of which are under user control. A rough rule of thumb is that the number of independently resolvable spatial resolution elements available for velocity extraction is a few per fringe.

### B. Velocity measurement accuracy and detection limit

We estimate that the uncertainty in the fringe phase is around  $\pm 0.05$  fringe, or about  $\pm 0.3$  rad. This is based on careful comparisons of reduced data extracted from simultaneous recordings taken at low and high sensitivities. The origin of this uncertainty is systematic, inherent to the re-

cording method, and is present independent of the method of phase extraction. This is because data reduction techniques for extracting the phase from the fringe comb have to assume that the background functions  $A$  and  $B$  are slowly varying in a spatial sense. In almost all practical situations, this assumption is approximate because of the presence of high-frequency spatial noise, for example, from the speckle, and because of discontinuities in the spatial phase patterns for many types of data (e.g., across stepped target structures). Within the context of the FTM, there exists spectral content contributed by these various background and noise sources at frequencies close to the carrier frequency, this causes apparent mixing of phase and amplitude terms, and contaminates the extracted phase. Schemes have been proposed to improve this situation,<sup>47</sup> but these require separate calibrations and assumptions that are incompatible with our experiments. The only way to reduce this uncertainty is to employ a more sophisticated data recording scheme (similar to phase-stepping techniques) in which multiple (at least three) phase-shifted versions of the interferogram are simultaneously recorded to allow algebraic cancellation of most of the background noise sources. The push-pull quadrature VISAR recording scheme of Hemsing<sup>18</sup> is in this class and has become the accepted standard VISAR recording method for discrete channel recording. Hemsing demonstrated a line-imaging push-pull quadrature recording technique;<sup>20</sup> however, the scheme is significantly more complicated and difficult to implement than the single-frame method. It is conceivable that a push-pull quadrature recording scheme can reduce the phase extraction error by an order of magnitude. However, to the best of our knowledge no push-pull quadrature line-imaging VISAR system is being used routinely in a production environment, because of its complexity. We anticipate a probable need for it as measurement precision improves in the future.

The moderate accuracy of the phase extraction from the fringe pattern requires sensitive interferometer settings to obtain high accuracy on Doppler shift measurements. For accurate measurements we choose settings such that one of the interferometers operates with a shift of around seven fringes. With the systematic uncertainty of  $\pm 0.05$  fringe, a data record containing a shift of seven fringes results in a relative uncertainty of  $0.05/7 < 1\%$  in the determination of the Doppler shift (velocity). Even with this strategy of large fringe counts, the phase extraction uncertainty remains the dominant contribution to the measurement uncertainty by a large factor (for example, the uncertainty in  $\tau$  is less than 0.1% for a 7 mm etalon, about ten times smaller than the phase extraction uncertainty). The  $\pm 0.05$  fringe uncertainty applied to the most sensitive VPF (60 mm etalon with  $\text{VPF}_0 = 0.86 \text{ km/s/fringe}$ ) gives a system detection limit  $\sim 0.04 \text{ km/s}$ , and 1% relative uncertainty can be achieved for velocities  $> 4.3 \text{ km/s}$ .

### C. Resolution of fringe ambiguities

With a few exceptions, almost all of the data recorded with the line-VISAR system at OMEGA contain discontinuous fringe shifts. A common situation that produces such discontinuities is when a strong shock breaks through a mo-



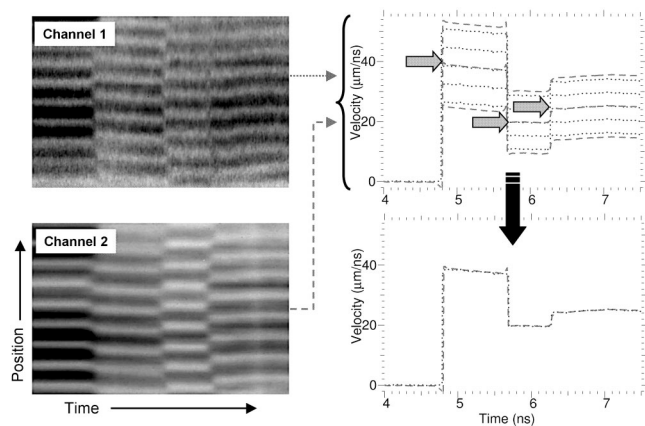


FIG. 7. Illustration of the resolution of fringe ambiguities. Channel 1 was operating with a 7 mm etalon ( $VPF_0=6.88$  km/s/fringe) and channel 2 with a 3 mm etalon ( $VPF_0=15.96$  km/s/fringe). The analyzed velocity profiles show a multitude of possible interpretations of the data based on one or the other of the two interferometers. Only one unique selection of possible fringe shifts produces close agreement for the Doppler shifts extracted from the two recordings.

tionless metal base plate into a transparent sample to produce a reflecting transmitted shock. The temporal resolution of the streak camera (about 10–50 ps depending on the sweep rate) is usually not fine enough to resolve the rapid fringe motion during the transition time  $\tau$  of the interferometer (about 15–50 ps), so the recorded pattern is discontinuous. As noted in Sec. V B, the fringe discontinuities can amount to as many as six or seven fringes plus a fractional part. For some kinds of experiments it may not be possible to determine reliably the integer part of the fringe shift from the data alone; this results in a fringe ambiguity. A reliable method to resolve fringe ambiguities is to record the data simultaneously on two separate interferometers with different sensitivities. This is the primary reason for the dual interferometer setup. With this arrangement, analysis and comparison of the data sets from both channels will lead to a unique determination of the Doppler shift, and resulting velocity. Typically, we choose the sensitivities such that the one channel is recording data between 2.5 and 3.5 fringes, while the second channel records at a shift of between six and eight fringes; this corresponds to a ratio of sensitivities ranging from 2:1 to 2.5:1 (e.g., a typical configuration employs 7 and 3 mm etalons).

Figure 7 illustrates the process of resolving the fringe ambiguities arising from a nontrivial sequence of discontinuities: a shock that is transmitted from an opaque pusher into a transparent fluid sample, reflected from a transparent anvil, then overtaken by a reverberation. Different fringe shifts must be applied at all of the discontinuities and different VPFs must be applied within the different media (sample and anvil) in order to reconstruct the velocity history. The top right panel in Fig. 7 shows the possible velocity histories that are consistent with the raw data for a sequence of three possible choices of fringe offsets for channel 2 (spaced by single fringes, dashed curves), and five choices for channel 1 (also spaced by single fringes, solid curves). In the absence of the information from the second interferometer a multitude of interpretations are possible, and one must introduce

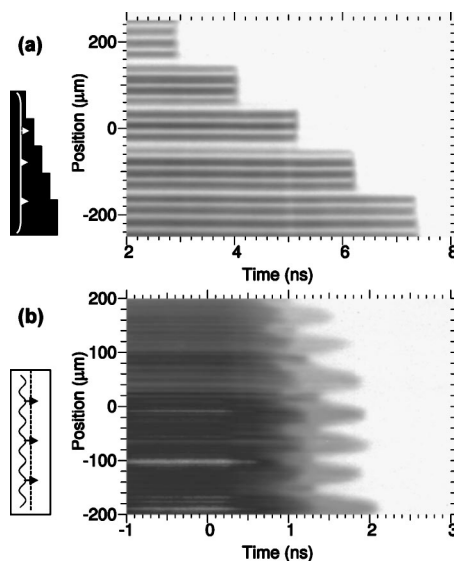


FIG. 8. (a) Shock breakout from a series of steps in an opaque metal target. Lack of fringe motion indicates the absence of preheat effects during this experiment. Shock velocity can be determined from the breakout times and the known step heights. (b) Shock breakout events in 20- $\mu$ m-thick plastic foil with an embedded Al layer driven by a modulated pressure drive. The fringes were removed by blocking one arm of the interferometer.

additional information to resolve the ambiguities. (Alternatively, one can use a single interferometer with low sensitivity such that fringe shifts are  $\sim 1$  fringe.) By combining the information from a dual interferometer setup no additional information is needed: matches between the two recordings are obtained for a unique set of integer fringe offsets, leading to a uniquely determined velocity profile shown in the bottom right of the figure.

## VI. SYSTEM OPERATION

Operation of the active shock breakout system is aided by the fact that it makes available, through the video CCD cameras, near-real-time images of the target as seen by the diagnostic during alignment and preshot operations. The probe laser sends out pulses at a 10 Hz rate, thus providing the experimenter and shot operations staff with an accurate indication of the alignment status of the target and the diagnostic at all times. The probe system is synchronized to the OMEGA master timing system so that one of the 10 Hz pulses is synchronous with the main laser shot. Prior to the main shot, test triggers are generated routinely to allow the cameras to record test sweeps (dry run tests) of the returned signal. This exercises the entire system up to and including the data recording stage. The streak cameras employ computer-controlled scientific-grade CCD readouts, to allow quick viewing of the test sweeps prior to the shot. These capabilities allow signal levels, fringe quality, alignment status, and trigger timing settings to be checked, adjusted, and tested prior to each shot. The system is therefore robust and reliable; failures caused by misalignment, mistiming, or poor signal quality are rare.

During the shot sequence the streak camera output detectors record three images: a background dark image (for subtracting CCD dark current background), a test image of

the stationary fringe pattern streaked prior to the shot, and finally the shot data. The first two images are recorded during the countdown sequence a few seconds before the main shot. The stationary fringe recording contains the background phase  $2\pi f_0 + \delta_0$ , and is therefore useful for background subtraction. It also provides a signal intensity reference that can be used to help analyze the data recording for target reflectance.

Between shots, the first element of the optical train (L1) is replaced, a task that results in slight shift ( $\sim 100$ – $200 \mu\text{m}$ ) of the pointing and focusing of the diagnostic. To adjust for this we usually place a reference grid at the location of the drive laser beams (which generate the pressure source for the shock), and align and focus the instrument to this reference. Following this step the experimental target is moved into the shot position.

## VII. EXPERIMENTS

### A. Breakout measurements

Figure 8(a) shows an example of a step breakout measurement of a uniform shock front propagating through a sequence of steps on an opaque metallic target. Breakout measurements of this type are typically required for performing impedance match equation of state experiments on metals or opaque materials at high pressures ( $>$  few times 100 GPa). Luminescence detection can provide equivalent information if the shock is strong enough; however, the reflection mode of detection is superior because the initial signal level can be set accurately near to the saturation level of the detector, and can provide the maximum possible dynamic range. The breakout time is accurately indicated because the reflection is extinguished to undetectable levels in a very short time interval,  $<30$  ps.<sup>13</sup> This is because the sample expands as an ionized plasma; once the profile has expanded to a scale length comparable to the probe wavelength, the reflectivity drops exponentially. (Reflections are not extinguished if the surface remains solid after the shock release; however, that motion can be detected as a fringe shift, described in the next section.)

The primary observables in this example are the breakout times; the presence of the fringes is not necessary for the measurement. (They can be removed by blocking one arm of the interferometer.) However, the velocity interferometer does provide secondary information if it is set sensitively enough to detect slight motions of the surface prior to the shock breakout. Such motion would indicate the presence of preheat, and is of concern to the experimenter. In this particular example no fringe motion is evident, indicating low or negligible preheat levels.

As a second example of breakout measurements, Fig. 8(b) shows the breakout patterns of a modulated shock passing through a uniform foil target. In this target, a  $0.5\text{-}\mu\text{m}$ -thick Al layer was embedded in the middle of a  $20\text{-}\mu\text{m}$ -thick polystyrene foil and the target was driven by a laser drive that was spatially modulated with a sinusoidal intensity variation of an approximately  $60 \mu\text{m}$  period. Breakout through the Al layer is seen first around 1 ns, when the reflected intensity is partially extinguished, followed by break-

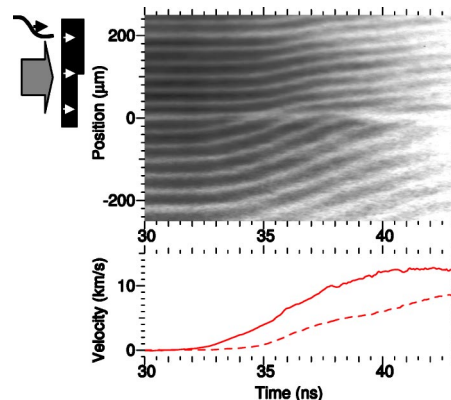


FIG. 9. Free surface motion on the rear surface of a stepped Al plate driven with a ramping (shockless) stress wave. The curves show the velocities extracted from the thin (solid curve) and thick (dashed curve) steps of the foil.

out out through the rear surface of the foil around 2 ns, when the reflection is fully extinguished. The variation in breakout times can be correlated directly to the spatially modulated pressure profile of the drive. In order to observe the modulated breakout clearly, the fringes were removed by blocking one arm of the interferometer. The high-frequency spatial intensity modulations are caused by the speckle distribution in the illumination beam. Further details of these experiments can be found in Ref. 48.

The accuracy of breakout measurements is limited by the performance of the streak camera, and by the accuracy of the sweep calibration. This varies depending on the settings of the camera; at the fastest sweep rates of over a few nanoseconds temporal window we achieve around  $\pm 20$  ps.

### B. Free surface and interface motion

The line-VISAR is especially useful for measuring the motion induced by low stresses in the elastic-plastic response range of many materials. These stresses usually leave the sample in the solid phase at relatively low temperatures (a few 100 K, undetectable with luminescence techniques), and are well suited to velocimetry because high surface reflectivities are maintained. Experiments in this class can be configured to observe a free surface directly, or by placing the reflecting interface behind a shock window in order to maintain impedance-matched wave propagation.

Figure 9 shows a recording of the motion of a thin-stepped Al foil driven by a shockless (slowly rising) pressure pulse.<sup>49</sup> The thin step ( $8.1 \mu\text{m}$ ) of the foil accelerates smoothly and continuously, while the thicker part ( $18.4 \mu\text{m}$ ) of the foil shows a later and slower acceleration. The observed accelerations correspond to peak stresses around 50 GPa (500 kbar) in the foil. These velocity measurements are essential for characterizing the pressure pulse driving the motion. For shockless drives, this type of measurement may be used quantitatively to determine isentropic compression curves for the target material.<sup>50</sup>

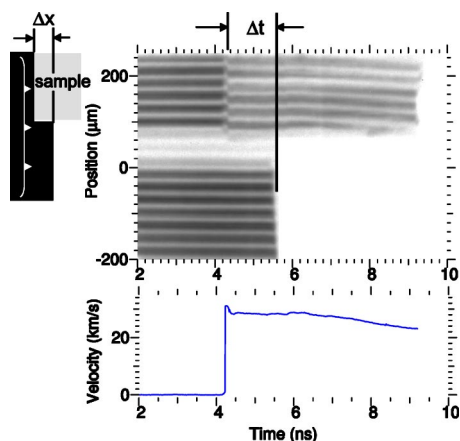


FIG. 10. Impedance matching EOS experiment, during which a shock is transmitted into the transparent sample through the lower step of a stepped Al baseplate. The lower frame shows the velocity of the shock front in the sample as determined from the fringe phase on the upper part of the recording. There is a brief ( $\sim 150$  ps) velocity transient when the shock is transmitted through an adhesive layer before entering the sample.

### C. Impedance matching equation of state in transparent samples

An important class of laser-driven shock experiments that has been enabled by the line-VISAR at OMEGA is the measurement of the equation of state (EOS) of transparent dielectric samples through impedance matching. The objective of such experiments is to determine the Hugoniot equation of state generated in a sample by transmitting a shock wave from a standard reference material into the sample material. The Hugoniot state in the sample can then be determined in a relative fashion through the known EOS of the reference material. Two primary observables are needed: (1) the shock velocity in the reference material ( $u_r$ ); and (2) the shock velocity in the sample ( $u_s$ ). The basic configuration of these experiments is shown in Fig. 10. In most of our experiments we use a stepped Al baseplate as the reference material:  $u_r$  can be determined from  $\Delta x / \Delta t$  (see Fig. 10), where  $\Delta x$  is the measured height of the Al step, and  $\Delta t$  the transit time of the shock across the step. The fringe shift is used to determine  $u_s$ ; this measurement presumes that the shock is strong enough to ionize the sample into a reflecting state in order for a return signal to be observed.

The line-VISAR technique provides a key advantage over step breakout measurements because it produces a continuous record of the shock velocity history. This is important because it provides an immediate assessment of the steadiness of the shock propagation in the sample. In this case shown in Fig. 10, the shock is steady during the measurement time, and begins to attenuate in the sample after  $t = 6$  ns. We have carried out such experiments in a number of dielectrics, including water, LiF, sapphire, diamond, polystyrene, fused silica, and alpha-quartz. Threshold pressures required to obtain high shock reflectivities vary widely among these materials; in most cases the pressures are too high to be accessible with conventional shock drivers (explosives and gas guns), but are well within the capabilities of large laser facilities such as OMEGA.

The measurement uncertainty of the Hugoniot state de-

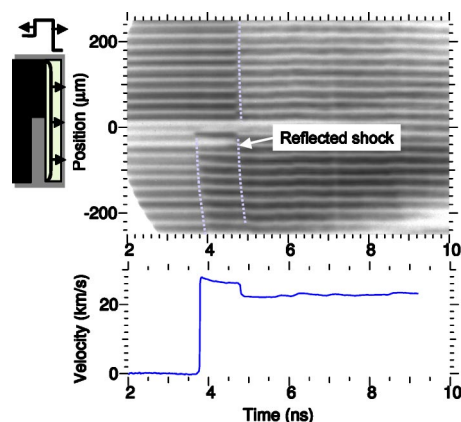


FIG. 11. Anvil reflected shock experiment: a shock incident in an Al plate is transmitted from the lower Al step into a transparent fluid sample (water) and then into a transparent anvil (fused silica). The anvil is attached to the upper step. The lower frame shows the shock velocities in the fluid sample and in the anvil.

pends on the uncertainties in measuring both  $u_r$  and  $u_s$ . As noted in Sec. VB the Doppler measurement uncertainty  $\Delta u_s / u_s \sim 1\%$  is of moderate accuracy, but still outperforms the accuracies attainable for the step breakout measurement ( $\Delta u_r / u_r \sim 2.5\%$  for the conditions allowed by OMEGA). As a consequence, the total uncertainty of impedance-matched EOS data measured at OMEGA is dominated by the contribution from the step breakout velocity measurement.

### D. Reflected shocks

For transparent materials, the line-VISAR is particularly useful for obtaining precise measurements of reflected shock events using transparent anvils. In these experiments a shock is transmitted from a transparent sample into a higher impedance anvil; the incident shock resolves into a transmitted and a reflected shock. In the example shown in Fig. 11, the impact occurs at  $\sim 4.8$  ns: just prior to this time the shock velocity in the sample (water) is  $25.4 \pm 0.3$  km/s and the shock transmitted into the anvil (fused silica) has a velocity of  $22.0 \pm 0.2$  km/s.

By measuring the incident shock velocity in the sample fluid and the transmitted shock state in the anvil, the double shock state in the fluid can be determined if the principal Hugoniot are known in both materials. The line-imaging technique has an advantage over conventional methods based on transit time measurements because the velocity measurement is localized both spatially and temporally, thus minimizing systematic errors associated with nonsteady and/or nonplanar propagation. We have carried out such experiments using water and liquid deuterium as sample fluids and alpha-quartz, fused silica, sapphire, and LiF as anvils. The example used to illustrate Figs. 6 and 7 shows a strong shock in liquid deuterium transmitted into an alpha-quartz anvil.

This technique may also be used to determine release states in transparent material by transmitting the shock from the sample into a lower impedance material.



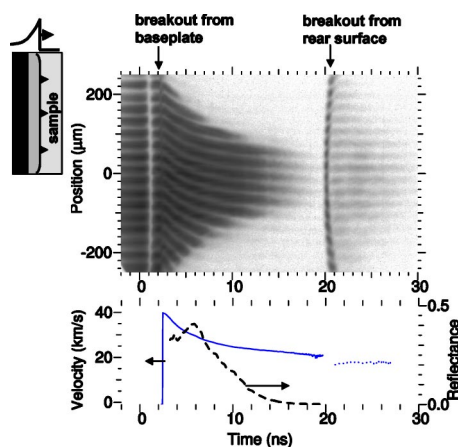


FIG. 12. Attenuating shock in diamond. In the lower frame are shown the velocity of the shock front (solid curve) and the velocity of the free surface of the diamond crystal after release (dotted curve). The reflectance of the shock front (dashed curve) is also shown on the same plot.

### E. Reflectivity of attenuating shocks

The line-imaging VISAR can provide valuable information on transport properties in shocked fluids because the fringe pattern encodes both the reflectivity and the velocity of the shock front. From this pair of observables it is possible to construct a quantitative relationship between the reflectance and shock velocity over a wide range of velocities in a single experiment. These experiments employ nonsteady attenuating shocks to sample the range of states. The initial drive pressure must be high enough (usually several 100 GPa) to create a dense hot conducting (metallic-like) fluid state. Even though the shock is nonsteady, the material at the leading edge of the shock front is always compressed to a state on the principal Hugoniot. The reflection originates within a skin depth of the metallic fluid, a distance of the order of 100 nm or less, over which the thermodynamic variables vary only slightly. Therefore, the observed reflectance represents a continuous sampling of states distributed at or very near to the principal Hugoniot through a wide range of pressures. This information is of value for inferring the variation of electrical conductivity and carrier density along the Hugoniot. This technique has been demonstrated in deuterium,<sup>27</sup> as well as in LiF and sapphire.<sup>28</sup>

Figure 12 shows an example of an attenuating shock in diamond. The shock was produced by driving a target comprised of a 20  $\mu\text{m}$  polystyrene ablator, a 50  $\mu\text{m}$  Al baseplate, and a  $\sim 250\text{-}\mu\text{m}$ -thick diamond plate. The target was driven by a 1 kJ pulse of 1 ns duration. X-rays generated in the laser plasma cause a brief period of photoionization in the diamond, rendering it partially opaque around  $t=1$  ns. The x-ray source terminates with the end of the laser pulse and the diamond sample becomes transparent again (through recombination of the photoionized electrons): the fringe pattern reappears unshifted at  $\sim 1.5$  ns.<sup>51</sup> The breakout from the baseplate at  $\sim 2.6$  ns is simultaneous across the 650  $\mu\text{m}$  spot, indicating that the shock is initially planar; however, it is attenuating because the applied pressure pulse is brief, and a rarefaction rapidly overtakes the leading shock front before it breaks out of the Al baseplate. Initially, the fringes are visible over the full diameter of the laser spot (650  $\mu\text{m}$ ).

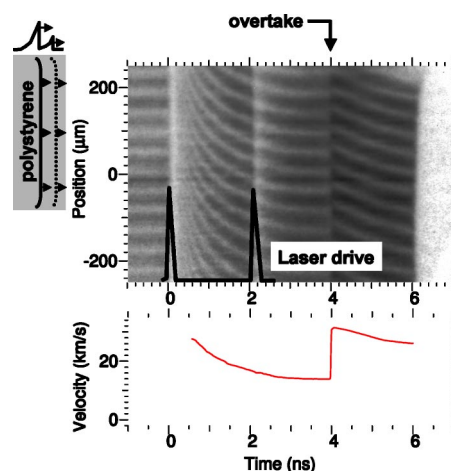


FIG. 13. Multiple attenuating shocks launched in a polystyrene sample by two short-duration, intense pulses separated by a 2 ns interval. The lower frame (solid curve) shows the velocity of the leading shock front.

Later, edge rarefactions move towards the central axis, causing loss of signal beyond the edges. The shock remains flat in the central 200  $\mu\text{m}$  for the duration of the recording. Here, the reduction in the signal is related to the intrinsic reflectivity of the shock front. (The probe laser beam was pulse-stacked to produce a  $\sim 30$  ns duration pulse for this experiment; details of this modification are not described in this article.)

Around 20 ns, the shock emerges from the rear surface. The curvature on the shock front is evident from the variation in breakout time across the diameter. The momentary discontinuity in fringe phase and intensity at the moment of breakout (detector-limited) is associated with the destruction of an antireflection coating on the rear surface; the persistence of the reflection for a few ns after the breakout indicates that the rear surface of the sample has released into the solid phase, thus retaining a sharp reflecting interface.

During this experiment the shock velocity initially launched in the diamond sample is  $\sim 40$  km/s corresponding to  $\sim 3900$  GPa (39 Mbar) pressure, and decays to  $\sim 20.5$  km/s,  $\sim 600$  GPa (6 Mbar). Corresponding temperatures and densities (estimated from theoretical EOS models) vary between 90 000 and 5000 K, and 10 and 6 g cm<sup>-3</sup>, respectively. The observed reflectivity is that of a dense, strongly coupled carbon plasma.

### F. Applications to inertial confinement fusion

Inertial confinement fusion (ICF) requires the control and timing of a series of shocks launched by a complex stepped driving pulse. For example, a shock timing scheme for the indirect drive form of ICF requires a sequence of three shocks to coalesce nearly simultaneously at a prescribed depth within the target fuel.<sup>52</sup> A line-imaging VISAR will be used for experiments to observe these shocks and to verify their relative timing behavior.

Figure 13 shows an example of an experiment designed to approximate a pulse delivery scheme for direct drive ICF. In this example, two attenuating shocks are launched into a target (polystyrene in this case), by applying a sequence of two brief intense laser pulses. X-rays generated by the sur-

face plasma created by the first pulse cause a brief period of photoionization in the target, which renders it partially opaque; it gradually relaxes to become more transparent, and the VISAR signal reveals an attenuating shock propagating through the target after about 0.4 ns. Between 0.4 and 4 ns the fringe pattern shows a strong continuous deceleration of the shock, as would be expected. The second laser drive pulse at 2 ns causes another loss of signal intensity (but the fringe phase remains continuous). The fringe discontinuity associated with this second shock is seen later at 4 ns, when the second shock overtakes the first. The fringe pattern terminates at 6 ns, when the shock breaks through the rear surface of the plastic target. Detailed comparison of these data with numerical models of the laser-target interactions will aid greatly in understanding the coupling of the laser to the target for these short intense pulses.

### VIII. DISCUSSION

The system described here has evolved out of experience with similar implementations fielded at various facilities, including NOVA, Vulcan, and Phebus. At OMEGA and these other facilities, variations and additions to the basic arrangement have been implemented that are not included in the description just presented. Four of the most useful variations include: (1) schemes to lengthen the duration of the probe pulse; (2) schemes for simultaneous dual wavelength operation, for example, at the fundamental (1064 nm) and second harmonic (532 nm) of the probe laser; (3) the addition of an optical recording channel using the existing imaging relay to record thermal luminescence data simultaneous with the VISAR data; and (4) the addition of dove prisms to enable arbitrary image orientation on the detector.

A line-imaging VISAR capability is currently being developed for the National Ignition Facility. Its design differs from the OMEGA implementation in many details, but benefited greatly by the experience gained with the VISAR implementation on OMEGA and its predecessors.

### ACKNOWLEDGMENTS

The authors wish to thank P. Bell, R. Costa, J. E. Cox, K. Haney of LLNL, G. Pien of LLE for help during the fabrication and installation of the instrument, D. H. Kalantar and K. T. Lorenz for providing the data in Fig. 9, and J. H. Eggert for useful discussions. In addition, we thank the operations staffs of both the NOVA and the OMEGA laser facilities. This work was performed under the auspices of the U.S. Department of Energy by Lawrence Livermore National Laboratory under Contract No. W-7405-ENG-48, and supported by the U.S. Department of Energy Office of Inertial Confinement Fusion under Cooperative Agreement No. DE-FC03-92SF19460, the University of Rochester, and the New York State Energy Research and Development Authority.

### APPENDIX: INTERFEROMETER ALIGNMENT

Following is the detailed procedure to align the interferometer. Using a plastic ruler, and with the delay etalon removed, the end mirror on the adjustable leg of the interferometer is set to a position to match the path of the fixed leg

within the accuracy of the ruler measurement (usually within 0.5 mm.) (1) The telescope line of sight is adjusted to view precisely through the aperture centers of IB2 and IM2 on the interferometer (see Figs. 3 and 4); this procedure is accomplished with the help of alignment aids placed at the IB2 and IM2 positions. (2) The angle of the beamsplitter IB2 is adjusted to center the aperture of IM1 as viewed through the telescope. (3) With reticle R2 placed at IB1 and the telescope focused on it the angles of IM1 and IM2 are adjusted to center the double image of R2 as viewed through both paths. (4) R2 is removed, the telescope is focused to the IB2 plane, and an image of reticle R1 is projected into the interferometer and also focused at the IB2 plane, where a double image is observed. (5) The angle of IB1 is adjusted to cause precise overlap of the double image at IB2. (6) Relative path difference is adjusted by translating the motorized mirror (no etalon) slowly (velocity  $< 2 \mu\text{m/s}$ ) until white light fringes appear in the image at the beam splitter plane IB2. The paths are matched by translating until the central fringe of the white light pattern is situated in the center of the image viewed by the telescope. Since each fringe represents approximately  $0.5 \mu\text{m}$  optical path difference, we estimate that the accuracy of matching the paths using this technique is  $\sim 1.5 \mu\text{m}$  (assuming the final fringe pattern is shifted by no more than two or three fringes away from the central fringe).

<sup>1</sup>L. Veaser and J. Solem, Phys. Rev. Lett. **40**, 1390 (1978).

<sup>2</sup>R. Trainor, J. Shaner, J. Auerbach, and N. Holmes, Phys. Rev. Lett. **42**, 1154 (1979).

<sup>3</sup>F. Cottet, J. P. Romain, R. Fabbro, and B. Faral, Phys. Rev. Lett. **52**, 1884 (1984).

<sup>4</sup>D. Parfeniuk, A. Ng, and L. Dasilva, Opt. Commun. **53**, 389 (1985).

<sup>5</sup>T. Lower *et al.*, Phys. Rev. Lett. **72**, 3186 (1994).

<sup>6</sup>P. Celliers, A. Ng, G. Xu, and A. Forsman, Phys. Rev. Lett. **68**, 2305 (1992).

<sup>7</sup>A. Benuzzi, T. Lower, M. Koenig, B. Faral, D. Batani, D. Beretta, C. Danson, and D. Pepler, Phys. Rev. E **54**, 2162 (1996).

<sup>8</sup>R. Kauffman *et al.*, Rev. Sci. Instrum. **66**, 678 (1995).

<sup>9</sup>J. Oertel *et al.*, Rev. Sci. Instrum. **70**, 803 (1999).

<sup>10</sup>A. Ng, D. Parfeniuk, P. Celliers, and L. DaSilva, in *Shock Waves in Condensed Matter-1985*, edited by Y. Gupta (Plenum, New York, 1986), pp. 255–260.

<sup>11</sup>A. Ng, D. Parfeniuk, P. Celliers, L. DaSilva, R. More, and Y. Lee, Phys. Rev. Lett. **57**, 1595 (1986).

<sup>12</sup>D. Parfeniuk, A. Ng, L. DaSilva, and P. Celliers, Opt. Commun. **56**, 425 (1986).

<sup>13</sup>M. Basko, T. Lower, V. N. Kondrashov, A. Kendl, R. Sigel, and J. Meyerter Vehn, Phys. Rev. E **56**, 1019 (1997).

<sup>14</sup>L. Barker and R. Hollenbach, Rev. Sci. Instrum. **36**, 1617 (1965).

<sup>15</sup>L. Barker and R. Hollenbach, J. Appl. Phys. **41**, 4208 (1970).

<sup>16</sup>L. Barker and R. Hollenbach, J. Appl. Phys. **43**, 4669 (1972).

<sup>17</sup>D. Goosman, J. Appl. Phys. **46**, 3516 (1975).

<sup>18</sup>W. Hemsing, Rev. Sci. Instrum. **50**, 73 (1979).

<sup>19</sup>D. Bloomquist and S. Sheffield, J. Appl. Phys. **54**, 1717 (1983).

<sup>20</sup>W. Hemsing, A. Mathews, R. Warnes, M. George, and G. Whittemore, in *Shock Compression of Condensed Matter-1991*, edited by S. Schmidt, R. Dick, J. Forbes, and D. Tasker (Elsevier, New York, 1992), pp. 767–770.

<sup>21</sup>K. Baumung, J. Singer, S. Razorenov, and A. Utkin, in *Shock Compression of Condensed Matter-1995*, edited by S. Schmidt and W. Tao (AIP, Woodbury, NY, 1996), p. 1015.

<sup>22</sup>W. M. Trott and J. R. Asay, in *Shock Compression of Condensed Matter-1997*, edited by S. Schmidt, D. Dandekar, and J. Forbes (AIP, Woodbury, NY, 1998), p. 837.

<sup>23</sup>P. Celliers, G. Collins, L. DaSilva, D. Gold, and R. Cauble, Appl. Phys. Lett. **73**, 1320 (1998).

<sup>24</sup>W. M. Trott, M. D. Knudson, L. C. Chhabildas, and J. R. Asay, in *Shock Compression of Condensed Matter-1999*, edited by M. D. Furnish, L. C.

- Chhabildas, and R. S. Hixson (AIP, Melville, NY, 2000), p. 993.
- <sup>25</sup>E. Moshe, E. Dekel, Z. Henis, and S. Eliezer, *Appl. Phys. Lett.* **69**, 1379 (1996).
- <sup>26</sup>D. M. Gold, P. M. Celliers, G. W. Collins, K. S. Budil, R. Cauble, L. B. da Silva, M. E. Foord, R. E. Stewart, R. J. Wallace, and D. Young, *Astrophys. J., Suppl. Ser.* **127**, 333 (2000).
- <sup>27</sup>P. M. Celliers, G. W. Collins, L. B. Da Silva, D. M. Gold, R. Cauble, R. J. Wallace, M. E. Foord, and B. A. Hammel, *Phys. Rev. Lett.* **84**, 5564 (2000).
- <sup>28</sup>D. Hicks, P. Celliers, G. Collins, J. Eggert, and S. Moon, *Phys. Rev. Lett.* **91**, 035502 (2003).
- <sup>29</sup>P. Loubeyre *et al.*, *High Press. Res.* **24**, 25 (2004).
- <sup>30</sup>D. Batani *et al.*, *Phys. Rev. Lett.* **88**, 235502 (2002).
- <sup>31</sup>E. Henry *et al.*, *Laser Part. Beams* **19**, 111 (2001).
- <sup>32</sup>A. Benuzzi-Mounaix *et al.*, *Phys. Plasmas* **9**, 2466 (2002).
- <sup>33</sup>Equation (1) is approximate because the beam passes through the etalon slightly obliquely at  $\theta=4.5^\circ$  angle of incidence. With oblique incidence and using the usual translation offset,  $d=h(1-1/n)$ , it can be shown that the exact expression for the delay is  $\tau^*(\theta)=(2h/c)[n/\cos\phi - 1/(n\cos\theta)]$ , where  $n\sin\phi=\sin\theta$ . A Taylor series expansion in  $\theta$  reveals that  $\Delta\tau/\tau=[\tau^*(\theta)-\tau]/\tau\sim O(\theta^4)$  and  $|\Delta\tau/\tau|<10^{-5}$  for our interferometer. Since our relative measurement uncertainty is  $\sim 1\%$ , Eq. (1) is accurate enough for our purposes.
- <sup>34</sup>Ideally, the required delay should be accomplished with a single element; if multiple elements are used it is advisable to use spacers to maintain an air gap  $>1$  mm between adjacent elements, in order to avoid thin-film interference effects causing reflections at the interface.
- <sup>35</sup>L. Barker and K. Schuler, *J. Appl. Phys.* **45**, 3692 (1974).
- <sup>36</sup>R. Setchell, *J. Appl. Phys.* **50**, 8186 (1979).
- <sup>37</sup>J. Wise and L. Chhabildas, in *Shock Waves in Condensed Matter-1985*, edited by Y. Gupta (Plenum, New York, 1986), p. 441.
- <sup>38</sup>S. Jones and Y. Gupta, *J. Appl. Phys.* **88**, 5671 (2000).
- <sup>39</sup>This sensitivity formula has been independently confirmed by measurements of shock propagation in liquid deuterium by M. D. Knudson, J. R. Asay, and others of Sandia National Laboratory, private communication M. D. Knudson.
- <sup>40</sup>W. Sweatt and O. Crump Jr., *Rev. Sci. Instrum.* **62**, 2946 (1991).
- <sup>41</sup>G. Fisk, G. Mastin, and S. Sheffield, *J. Appl. Phys.* **60**, 2266 (1986).
- <sup>42</sup>J. Slepicka and S. Cha, *Appl. Opt.* **34**, 5039 (1995).
- <sup>43</sup>M. Takeda, H. Ina, and S. Kobayashi, *J. Opt. Soc. Am.* **72**, 156 (1982).
- <sup>44</sup>W. J. Macy, *Appl. Opt.* **22**, 3898 (1983).
- <sup>45</sup>K. Nugent, *Appl. Opt.* **24**, 3101 (1985).
- <sup>46</sup>C. Roddier and F. Roddier, *Appl. Opt.* **26**, 1668 (1987).
- <sup>47</sup>J. Lui and P. Ronney, *Appl. Opt.* **36**, 6231 (1997).
- <sup>48</sup>T. Boehly, T. Collins, O. Gotchev, T. Kessler, J. Knauer, T. Sangster, and D. Meyerhofer, *J. Appl. Phys.* **92**, 1212 (2003).
- <sup>49</sup>J. Edwards *et al.*, *Phys. Rev. Lett.* **92**, 075002 (2004).
- <sup>50</sup>C. Hall, J. Asay, M. Knudson, W. Stygar, Spielman, T. Pointon, D. Reisman, A. Toor, and R. Cauble, *Rev. Sci. Instrum.* **72**, 3587 (2001).
- <sup>51</sup>Photoionization effects in transparent samples can be suppressed with more sophisticated target designs that employ x-ray-attenuating layers containing high-Z materials, for example, plastics doped with a few atomic % of Br or I.
- <sup>52</sup>D. Munro, P. Celliers, G. Collins, D. Gold, L. Da Silva, S. Haan, R. Cauble, B. Hammel, and W. Hsing, *Phys. Plasmas* **8**, 2245 (2001).